Flow, Turbulence and Combustion manuscript No.
(will be inserted by the editor)

Effects of the actuation on the boundary layer of an airfoil at Reynolds number $Re = 60000$

Ivette Rodriguez · Oriol Lehmkuhl* · Ricard Borrell

April 30, 2020

Abstract Synthetic (zero net mass flux) jets are an active flow control technique to manipulate the flow field in wall-bounded and free-shear flows. The present paper focuses on the role of the periodic actuation mechanisms on the boundary layer of a SD7003 airfoil at $Re = U_\infty C/\nu = 6 \times 10^4$. Here, Reynolds number is defined in terms of the free-stream velocity U_∞ and the airfoil chord C. The actuation is applied near the leading edge of the airfoil and is periodic in time and in the spanwise direction. The actuation successfully eliminates the laminar bubble at $AoA = 4^\circ$, however, it does not produce an increase in the airfoil aerodynamic efficiency. At angles of attack larger than the point of maximum lift, the actuation eliminates the massive flow separation, the flow being attached to the airfoil surface

I. Rodriguez

Universitat Politècnica de Catalunya (UPC), Colom 11, ESEIAAT, 08221 Terrassa, Spain
E-mail: ivette.rodriguez@upc.edu

O. Lehmkuhl* · Ricard Borrell

Barcelona Supercomputing Center (BSC) E-mail: *(Corresponding author) oriol.lehmkuhl@bsc.es,ricard.borrell@bsc.es

in a significant part of the airfoil chord. As a consequence, airfoil aerodynamic efficiency increases by a 124% with a reduction of the drag coefficient about 46%. This kind of technique seems to be promising at delaying flow separation and its associated losses when the angle of attack increases beyond the maximum lift for the baseline case.

Keywords LES, flow control, synthetic jets

1 Introduction

Active flow control has been subject of many investigations due to its potential for controlling boundary layer flow separation and drag reduction. Different techniques for manipulating the boundary layer can be found in the literature such as suction and blowing devices (Kim et al. 2017, Zhu et al. 2019, Liu et al. 2010, Eto et al. 2018, Atzori et al. 2018), plasma actuators (Choi et al. 2011, Zheng et al. 2018), traveling waves (Albers et al. 2019, Akbarzadeh & Borazjani 2019), among others. Synthetic (zero net mass flux) jets are an active flow control technique to manipulate the flow field in wall-bounded and free-shear flows. The fluid necessary to actuate on the boundary layer is intermittently injected through an orifice and is driven by the motion of a diaphragm located on a sealed cavity below the surface Glezer (2011). Comprehensive reviews on active flow control techniques can be found in Glezer (2011) and Cattafesta & Sheplak (2011).

Periodic excitation introduced at the surface has been shown as an efficient and practical means of flow control, with the potential to significantly change the lift and drag of an airfoil and the separation of the boundary layer. In the particular case of synthetic jets, there are different parameters that control the actuation such

as the jet momentum coefficient ($C_\mu = h(\rho U_{max}^2)_{jet}/C\rho U_\infty^2$ defined as in Gilarranz et al. (2005*a*), where h is the width of the actuator neck, ρ the fluid density, U_{max} the maximum outlet velocity, C the airfoil chord and U_∞ the free-stream velocity), the slot position, the jet frequency (see for instance McCormick (2000), Amitay & Glezer (2002), Gilarranz et al. (2005*a*)). McCormick (2000) studied the effect of the jet momentum coefficient and observed that over a range of 0.0005-0.005 the airfoil aerodynamic efficiency increased by extending the stall angle up to 5-6deg. Goodfellow et al. (2013) studied the influence of the momentum coefficient of synthetic jets installed in a NACA 0025 at a $Re = U_\infty C/\nu = 10^5$ and a low angle of attack (AoA) $AoA = 5^\circ$. They found that above a determined value of momentum coefficient, the flow reattached to the surface thus reducing the wake width and the drag coefficient.

For the jets location, it has been suggested that this flow control mechanism is more effective if applied upstream flow separation. For instance, Amitay et al. (2001) investigated the use of synthetic jets to prevent separation in an unconventional symmetric airfoil with a round leading edge. By applying the flow control upstream separation they found a dramatic increase in the lift and a reduction of the drag for angles of attack larger than the stall angle. Moreover, they observed that depending on the actuation frequency the control effectiveness also varied.

Regarding periodic actuation, it has been reported two different ranges of non-dimensional frequency, $F^+ = f\,L/U_\infty$ (where f is the periodic actuation frequency and L is a characteristic length usually defined as the distance from the actuator to the trailing edge or the airfoil chord) in which actuation has been considered optimal, i.e. at $F^+\mathcal{O}(1)$ and at $F^+\mathcal{O}(10)$. Amitay & Glezer (2002) studied the effect of the actuation over a stalled airfoil and found that high actuation frequencies

suppressed the large scale vortical structures with a complete flow reattachment, whereas for actuation frequencies in the order of $F^+ = 1$ the reattached flow behaved unsteadily. Gilarranz et al. (2005*a*,*b*) (in two papers) found that the actuation frequency in the order of $F^+ = 1$ increases the magnitude of the lift and produces a reduction of the drag coefficient. Tuck & Soria (2008) experimentally investigated the effect of the wall normal actuation at the leading edge of a NACA 0015 at $Re = 3 \times 10^4$ with $F^+ = 1.3$. They showed that this kind of actuation can effectively control separation and increase the lift coefficient, thus delaying the stall of the airfoil. Later, Kitsios et al. (2011) using large-eddy simulations and by means of a linear stability analysis identified that the forcing frequencies in Tuck & Soria (2008) correspond with the wake frequency of the unforced flow. This was also confirmed experimentally by Buchmann et al. (2013).

From a numerical point of view, the accurate prediction of the flow over an airfoil is a challenging task as it is dominated by separation, transition to turbulence and, at some angles of attack, reattachment of the flow, not to mention the flow control mechanism. Several investigations have been conducted using RANS concerning the use of synthetic jets. For instance, Huang et al. (2004) performed a numerical study on a NACA 0012 at $Re = 5 \times 10^5$ and $AoA = 18^\circ$ to study the role of the suction and blowing, separately. They explored different parameters such as the position of the jet, its amplitude and its angle. Duvigneau & Visonneau (2006) studied the stall control by an automatic optimisation procedure of a NACA 0015 at $Re = 8.96 \times 10^5$ and found an increase in the lift and a delay of the stall for the optimum parameters. However, the complex nature of the unsteady flow over an airfoil is very difficult to be predicted by using RANS. In this sense, large-eddy simulations (LES) offer a good compromise between accuracy and computational

time required for performing the simulations. You & Moin (2008) successfully reproduced the control conditions of the experiments performed by Gilarranz et al. (2005*a*) and proved that LES techniques can be successfully applied for capturing the flow physics in these configurations. More recently, the simulations performed by Kitsios et al. (2011) have also shown that LES can be a powerful tool for analysing the flow and the excitation frequencies of synthetic jets.

The present paper focuses on the particular range of low Reynolds numbers for which the development of Micro Air Vehicles (MAV) is of interest ($Re < 5 \times 10^5$ Mueller & DeLaurier (2003)). At these Reynolds numbers, at low angles of attack the flow is affected by the formation of a laminar separation bubble (LSB), thus, its reduction or suppression is of importance when it comes to improve the airfoil aerodynamic efficiency. Moreover, when the angle of attack increases, the LSB bursting (Alam & Sandham 2000) leads to the airfoil stall. Thus, a large recirculation zone that severely affects the airfoil aerodynamic efficiency is formed. This is the case of the SD7003 airfoil. Actually, according to Selig et al. (1995), the SD7003 was designed to have a very long and gradual bubble ramp with low drag due to the LSB. However, at angles of attack larger than the point of maximum lift a large recirculation zone appears in the suction side; hence, the control of the flow at these angles is of interest. In this sense, the role of a periodic actuation, by means of synthetic jets, on the boundary layer of a SD7003 airfoil at $Re = 6 \times 10^4$ is investigated. This paper also investigates whether the periodic actuation is capable of delaying the stall and reducing the adverse effects of the separated zone at post-stall angles of attack. To do so, angles of attack of $AoA = 4^\circ$, 11°, and 14° are considered. The first one corresponds with an AoA with a large laminar separation bubble, the second one is close to the point of

maximum lift, whereas the last one corresponds with the flow in full stall. This is an attempt to understand the actuation mechanism on the boundary layer and the data obtained from the simulations can be further used for the development of low-order models.

2 Mathematical and numerical modelling

In this work, large eddy simulations (LES) of the flow are performed. The spatially filtered incompressible Navier-Stokes equations can be written as

$$\frac{\partial \overline{u}_i}{\partial x_i} = 0 \tag{1}$$

$$\frac{\partial \overline{u}_i}{\partial t} + \frac{\partial \overline{u}_i \overline{u}_j}{\partial x_j} - \nu \frac{\partial^2 \overline{u}_i}{\partial x_j \partial x_j} + \rho^{-1} \frac{\partial \overline{p}}{\partial x_i} = -\frac{\partial \mathcal{T}_{ij}}{\partial x_j} \tag{2}$$

where x_i (or x, y and z) are the spatial coordinates in the stream-wise, cross-stream and span-wise directions; t is the time. $\overline{u}_i$ (or u, v, w) and $\overline{p}$ are the filtered velocity components and pressure, respectively. ν and ρ are the kinematic viscosity and the fluid density. The term $\mathcal{T}_{ij}$ in the right hand side of equation 2 is the subgrid scale (SGS) stress tensor, which results from the unresolved subgrid-scale contributions and needs to be modelled. Its deviatoric part,

$$\mathcal{T}_{ij} - \frac{1}{3}\mathcal{T}_{kk}\delta_{ij} = -2\nu_{sgs}\overline{\mathcal{S}}_{ij} \tag{3}$$

where $\overline{\mathcal{S}}_{ij} = \frac{1}{2}\left(\partial \overline{u}_i/\partial x_j + \partial \overline{u}_j/\partial x_i\right)$ is the large-scale rate-of-strain tensor, and δ_{ij} is the Kronecker delta. ν_{sgs} is the subgrid scale viscosity; it is here modelled using Vreman (2004) SGS model.

Numerical simulations are performed using the code Alya (Vázquez et al. 2016). In Alya, equations are solved by means of a low-dissipation finite-element method

(FEM) (Lehmkuhl et al. 2019). The convective term is discretised using a Galerkin FEM scheme recently proposed by Charnyi et al. (2017), which conserves linear and angular momentum, and kinetic energy at the discrete level. Neither upwinding nor any equivalent momentum stabilisation is employed. In order to use equal-order elements, numerical dissipation is introduced only for the pressure stabilisation via a fractional step scheme (Codina 2001), which is similar to approaches for pressure-velocity coupling in unstructured collocated finite-volume codes. The set of equations is integrated in time using a third-order Runge-Kutta explicit method combined with an eigenvalue-based time-step estimator (Trias & Lehmkuhl 2011). This methodology has successfully been used in complex problems, e.g. Mira et al. (2016), Calmet et al. (2016), Gövert et al. (2017), Pastrana et al. (2018), Rodriguez et al. (2019).

2.1 Definition of the cases and boundary conditions

As mentioned in the introduction, large-eddy simulations of the flow around a SD7003 airfoil at Reynolds number $Re = U_\infty C/\nu = 6 \times 10^4$ at $AoA = 4^\circ$, 11° and 14° are performed. For each of these cases both the un-actuated (baseline) and the actuated cases are simulated. Solutions are obtained in a computational domain of dimensions $15C \times 16C \times 0.2C$ as is shown in figure 1. The inlet of the domain is located at $5C$ from the airfoil leading edge, whereas the outlet is placed at $9C$ from the airfoil trailing edge; the leading edge of the airfoil is at $(x,\ y,\ z) \equiv (0,\ 0,\ 0)$. In the spanwise direction a length of $L_z = 0.2C$ is used. This size is chosen considering previous results obtained in a NACA 0012 (Rodríguez et al. 2013) at a comparable $Re = 5 \times 10^4$, where it was shown that for post-stall

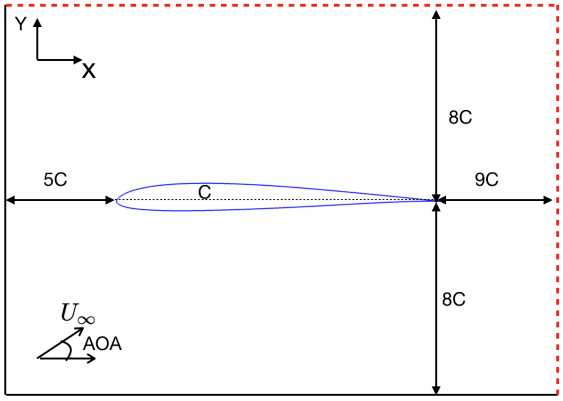

Fig. 1: Computational domain (not to scale). Black solid lines represent inflow conditions; red dashed lines represent outflow conditions.

AoAs, a spanwise size of $L_z = 0.2C$ was enough so as to contain the largest scales of the flow. Moreover, Galbraith & Visbal (2008) for the present configuration at $AoA = 4^\circ$ analysed the spanwise size in the range of $L_z/C = 0.1 - 0.3$ and observed minor differences among them, concluding that a size of $L_z = 0.2C$ was adequate for the simulations. For the actuated cases, as these simulations cover a range of AoA from $AoA = 4^\circ$ with a LSB to a post-stall situation ($AoA = 14^\circ$), and considering that boundary layer separation moves towards the leading edge as the AoA increases, the actuator line is located prior boundary layer separation, at $x/C = 0.007$; the actuation line width being $h/C = 0.007$.

The boundary conditions at the inflow consist of a uniform velocity profile (u, v, w)=($U_\infty \cos AoA$, $U_\infty \sin AoA$, 0). As for the outflow boundary, a pressure-based condition is imposed; being u_n the normal velocity at the outlet of the domain and γ an expansion coefficient, the outlet pressure results from the expression $p - 0.5\gamma\rho u_n^2 = 0$. In this work, $\gamma = 1$ is used. At the airfoil surface, a no-slip

condition is prescribed. Periodic boundary conditions are used in the spanwise direction. For the actuated cases, a periodic in time and in space inlet velocity at the outlet of the actuator line and normal to the airfoil surface is imposed as,

$$(u, v, w)_{act} = A_p U_\infty sin(2\pi f t) sin(2\pi \tau z)(\sin\alpha, \cos\alpha, 0) \tag{4}$$

Here, A_p is the maximum amplitude of the jet so as $U_{max} = A_p U_\infty$, f is the actuator frequency so as $F^+ = fU_\infty/x_{TE}$. Here, the non-dimensional frequency is defined as in Gilarranz et al. (2005*a*) in terms of x_{TE}, i.e. the x-distance from the actuator to the trailing edge. τ is the spanwise period of the signal, in this work $\tau = 0.5L_z$. α is the angle of the surface normal with the y-axis. The synthetic jet is also characterised by the momentum coefficient C_μ. According to McCormick (2000), in the range of $C_\mu = 5\times10^{-4}-5\times10^{-3}$, the increase in momentum coefficient increases the post-stall lift; this is also in agreement with the conclusions of Goodfellow et al. (2013) which observed that in the range of $C_\mu = 3.09\times10^{-3}-6.79\times10^{-3}$ the wake width was reduced for $AoA = 5^\circ$. Thus, in the present simulations, a momentum coefficient $C_\mu = 3 \times 10^{-3}$ is imposed. Moreover, the non-dimensional actuation frequency is $F^+ = 1$, for all cases.

2.2 Numerical grid

The computational meshes used are unstructured grids of about 29.94 and 30 million gridpoints for the baseline and the actuated cases, respectively. Both computational meshes are similar in terms of grid resolution and only minor differences are encountered in the zone where the actuator outlet is located. For obtaining these meshes, an unstructured two-dimensional mesh is extruded in $N_{elements}$ in

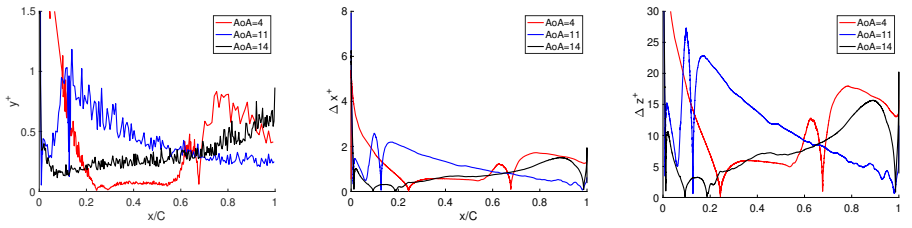

(a) (b) (c)

Fig. 2: Near wall grid resolution for the baseline cases. (a) Wall-normal distance of the first grid point off the wall, y^+ (b) arc-length streamwise Δx^+ (solid lines) and (c) spanwise Δz^+ (dashed lines) grid spacing.

the spanwise direction. The number of elements in the spanwise direction in all computations is 64. In all cases, the meshes are constructed so as in the near wall region the non-dimensional wall normal distance $y^+ = u_\tau\, y_n/\nu \approx 1$; y_n is the wall-normal distance and u_τ is defined in terms of the wall-normal shear stresses $u_\tau = \sqrt{\tau_w/\rho}$. In a similar way, the arc-length streamwise Δx^+ and spanwise Δz^+ resolutions are determined. In figure 2, the averaged values of the y^+, Δx^+ and Δz^+ along the airfoil suction side for the baseline cases are plotted. Moreover, in the near wake, i.e. $1 \leqslant x/C \leqslant 3$; $-0.4 \leqslant y/C \leqslant 0.8$, the meshes have been constructed clustering more gridpoints so as in this region the average ratio of the grid size h ($h \equiv \Omega^{1/3}$, Ω being the cell volume) to the Kolmogorov scale ($\eta = (\nu^3/\epsilon)^{1/4}$) is about $h/\eta \approx 10.8$, with maximum values about $(h/\eta)_{max} \approx 15$. Here, to evaluate the local Kolmogorov length scale the turbulent kinetic energy dissipation is approximated as $\epsilon = 2(\nu + \nu_{sgs})\overline{S'_{ij}S'_{ij}}$, S'_{ij} being the fluctuating strain rate.

In order to validate the current numerical set-up, the solution for the baseline cases are compared to available solutions in the literature. For the comparison,

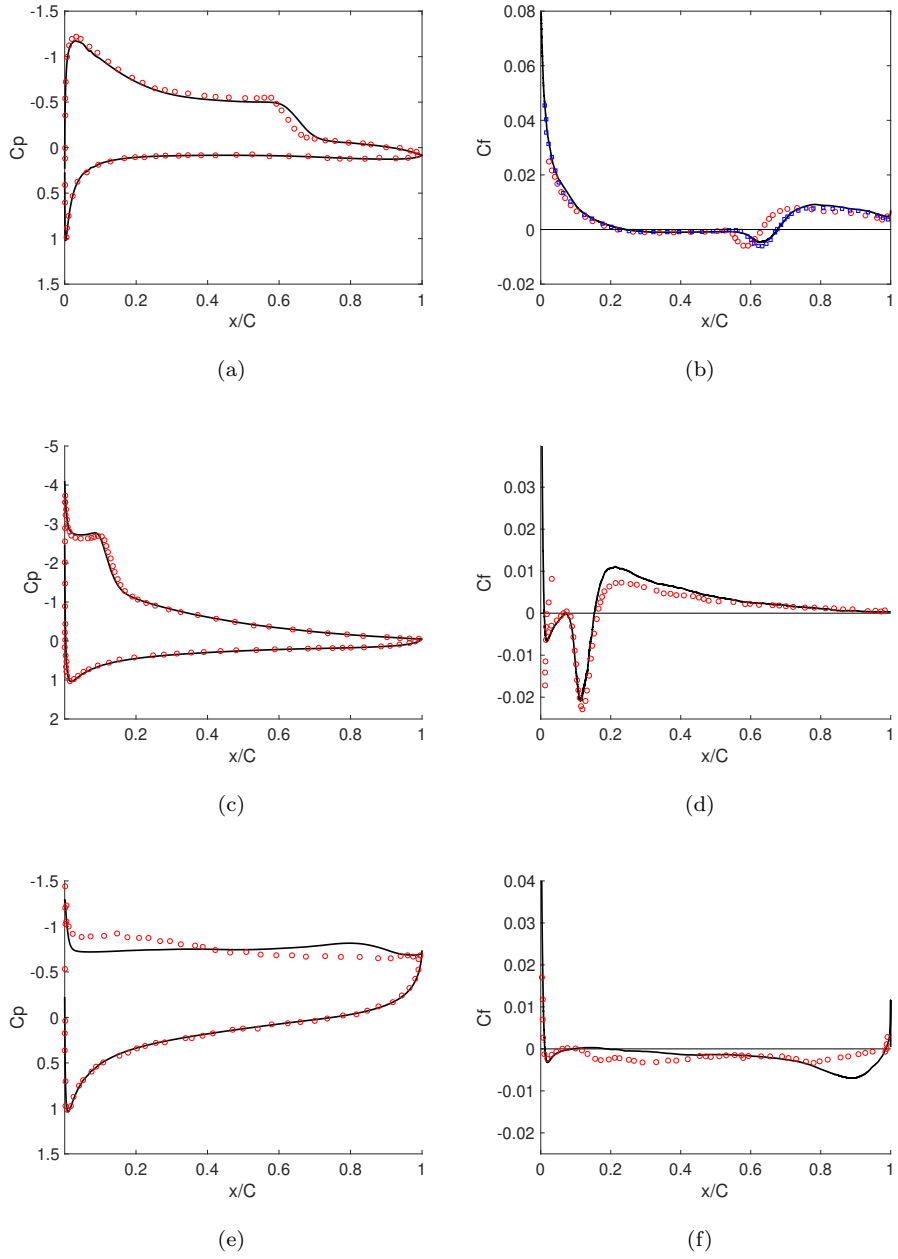

Fig. 3: Baseline case. Pressure coefficient for the upper and lower surfaces of the airfoil, C_p (left column) and skin friction coefficient at the upper surface of the airfoil, C_f (right column) for the different angles of attack. (a, b) $AoA = 4^\circ$, (c, d) $AoA = 11^\circ$, (e, f) $AoA = 14^\circ$. Comparison with the literature, (solid line) present LES results, (red circles) ILES (Galbraith & Visbal 2008), (blue squares) LES skin friction data at $AoA = 4^\circ$ by (Schmidt & Breuer 2014)

.

the results obtained by Galbraith & Visbal (2008), who performed implicit LES calculations at these AoA using a computational mesh of about 5.7 million of grid points are used. Additionally, the skin friction coefficient at $AoA = 4^\circ$ reported by Schmidt & Breuer (2014) using a mesh of 17.2 million of grid points and the dynamic model is also included in the comparison. In figure 3, both pressure coefficient $C_p = (p - p_\infty)/(0.5\rho U_\infty^2)$ and skin friction $C_f = \tau_w/(0.5\rho U_\infty^2)$ are reported. As can be seen from the figure, in all cases results are in good agreement with those of the literature. Notice that larger deviations with the ILES of Galbraith & Visbal (2008) are observed for $AoA = 14^\circ$, which is the most demanding situation with the flow fully detached from the airfoil surface. These differences might not only be attributed to the differences in the numerical method, but also to the computational meshes used.

3 Results and discussion

In this section, the effects of the periodic actuation on the flow, aerodynamic coefficients and on the the laminar separation bubble at $AoA = 4^\circ, 11^\circ$ are studied by comparing the local pressure coefficient and skin friction. Moreover, the impact of the actuation at the larger angle of attack, i.e. $AoA = 14^\circ$, where the flow is massively separated is also examined. In addition, the instantaneous and averaged flow are analysed at all angles of attack. For presenting the results, the baseline simulations have been started from an initially homogeneous flow field and have been run for about 20 time-units ($t\,U_\infty/C$) up until the initial transient has been washed out. Then, data have been collected for about 30 time-units for $AoA = 4^\circ$ and 11°, and for about 45 time-units for $AoA = 14^\circ$. To verify convergence, the lift

coefficient over the last half of the averaging period has been compared to the value over the whole simulation. Differences have been kept within 0.5% for all cases but the baseline at $AoA = 14^{\circ}$, where due to the massive separation fluctuations are larger and thus differences are less than 3%. In order to save some computational time, the actuated cases have been initialised from interpolated maps obtained from the baseline cases and have been run up until the statistical stationary state has been reached. Then, data have been collected for about 30 time-units for all angles of attack; the results presented have been averaged both in time and in the spanwise direction.

3.1 Effect of the actuation on the aerodynamic coefficients

To understand the effects of the actuation on the flow aerodynamic coefficients, the characteristics of the instantaneous flow at the different angles of attack for the baseline and actuated cases are analysed. In figure 4, the instantaneous vortical structures identified by means of the *Q-criterion* (Hunt et al. 1988) are presented. Q-isocontours coloured by the velocity magnitude are plotted in the figure for all cases considered. For the baseline cases, at $AoA = 4^{\circ}$ (figure 4a), due to the adverse pressure gradient the flow separates laminarly close to the leading edge of the airfoil at about $x/C = 0.24$; Kelvin-Helmholtz (KH) instabilities develop in the separated shear layer that trigger the transition to turbulence. After transition, the shear-stresses force the flow to reattach to the airfoil surface at about $x/C = 0.68$, thus forming a recirculation bubble also known as laminar separation bubble (LSB). After reattachment, the fully turbulent flow travels downstream to reach the airfoil trailing edge. As the angle of attack increases, the laminar boundary

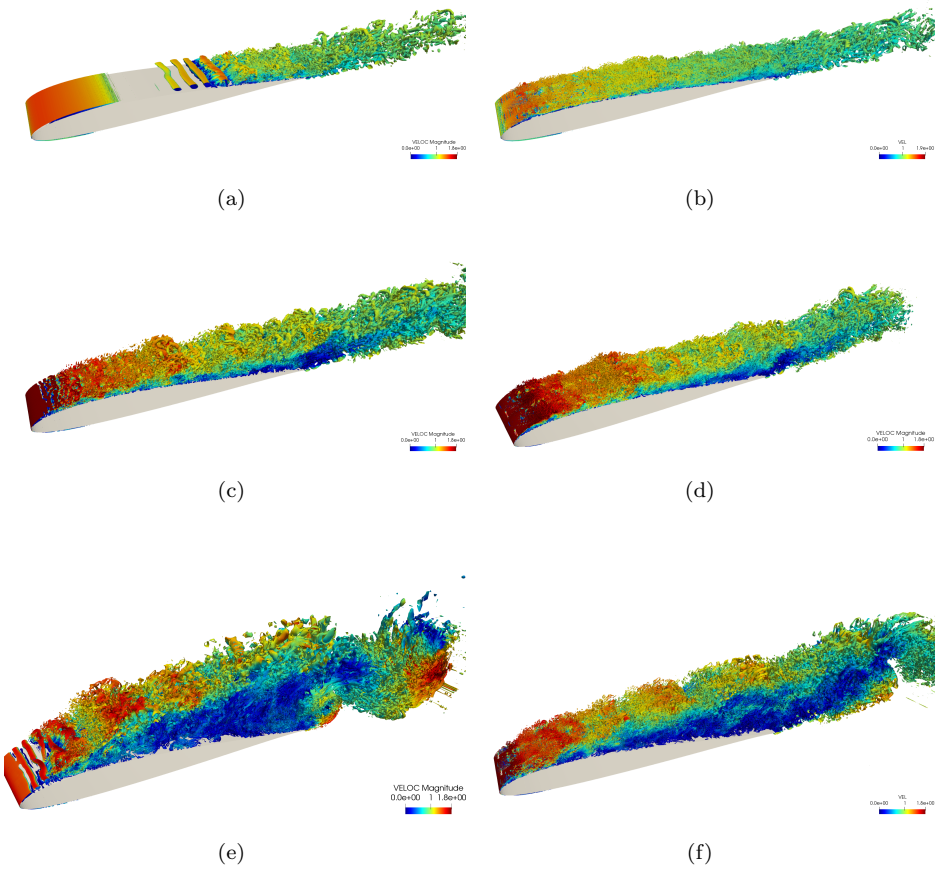

Fig. 4: Instantaneous vortical structures identified by means of Q-criterion $Q = 30\,U_\infty^2/C^2$ for the baseline (left column) and actuated (right column) cases: (a,b) $AoA = 4^\circ$, (c,d) $AoA = 11^\circ$, (e,f) $AoA = 14^\circ$

layer separation moves upstream and at $AoA = 11^\circ$ it is almost at the airfoil leading edge, at $x/C = 0.008$ (figure 4c). This angle of attack is close to the point of maximum lift at this Reynolds number, and transition to turbulence and flow reattachment also move towards the leading edge forming a small LSB. With the increase in the angle of attack the size of the LSB is reduced and, eventually, at

these Reynolds numbers the LSB burst and a drop in the lift coefficient occurs (Sandham 2008). A further increase in the angle-of-attack, $AoA = 14^\circ$ (figure 4e), the flow fails to reattach to the airfoil surface forming a large separated zone, and momentum deficit, along the suction side of the airfoil. As a result, the structures separated from the turbulent shear layer interact with the flow coming from the pressure side at the trailing edge shedding vortices behind the airfoil. The transient flow and vortex shedding process that occurs at a post-stall angle was described in detail for a NACA 0012 airfoil by Rodríguez et al. (2013).

The effect of the actuation on the pressure and skin friction coefficients is depicted in figure 5, where a comparison with the baseline cases is also plotted. When the periodic actuation close to the leading edge is activated, even at low angle of attack, transition to turbulence is triggered just downstream the actuator location (see figure 4b). Moreover, at $AoA = 4^\circ$, the actuation succeeds at suppressing the LSB, and thus the turbulent flow travels downstream forming an evolving turbulent boundary layer. These effects can also be seen by inspecting the pressure and skin friction profiles (see also figure 5a,b). The plateau in the pressure coefficient, typical of a LSB, is eliminated and a gradual pressure recovery is observed instead. Moreover a positive skin friction coefficient along the whole airfoil chord evidences that no flow separation occur at this AoA. When the angle of attack increases to $AoA = 11^\circ$ (figure 4d), even though the periodic actuation early triggers the transition to turbulence, the adverse pressure gradient forces the flow to separate; as a consequence a small recirculation zone is formed, but its smaller than the LSB formed at this angle-of-attack for the baseline case. The turbulent flow reattachment moves from $x/C = 0.15$ to $x/C = 0.09$ when the flow actuation is used

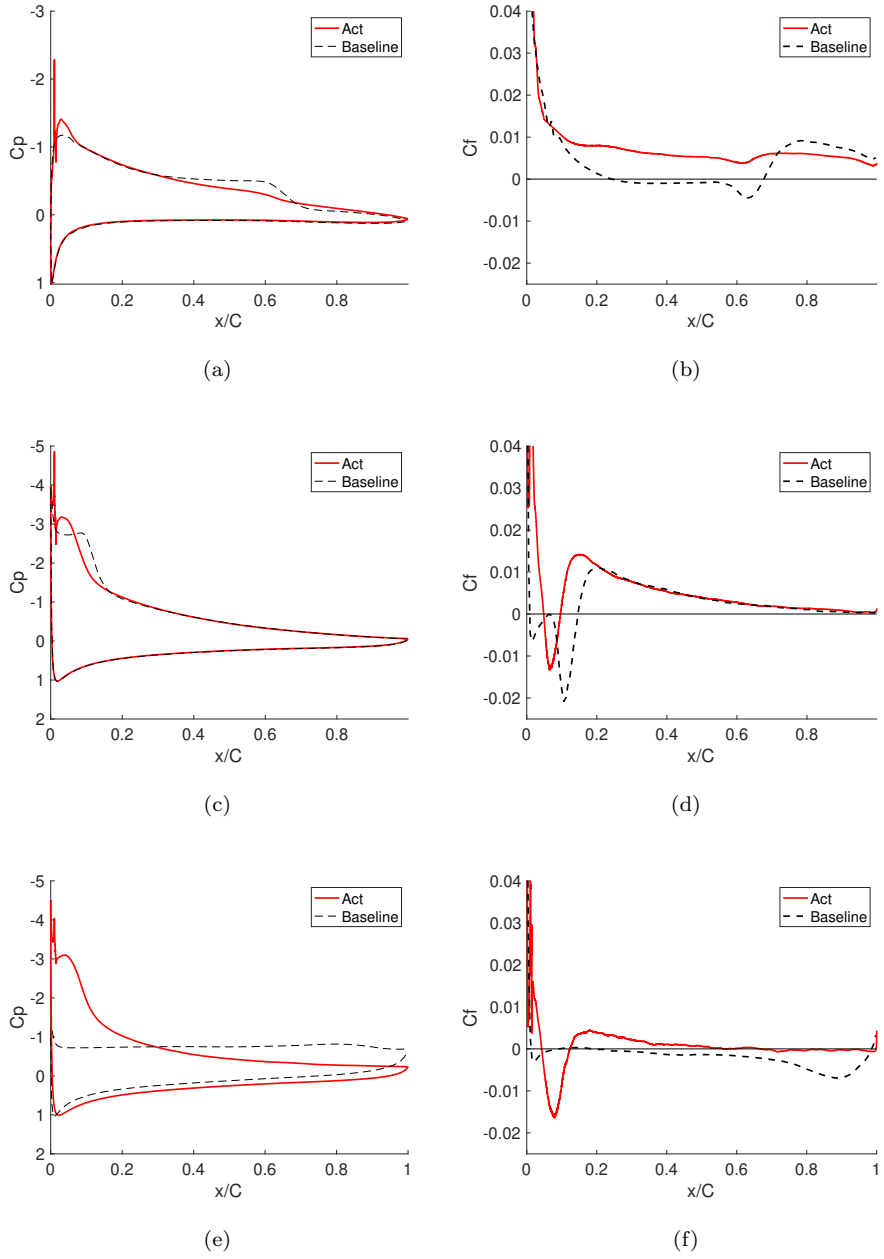

Fig. 5: Effect of the actuation on the pressure coefficient (left) and skin friction coefficient (right), comparison with the baseline case. (a,b) $AoA = 4^{\circ}$; (c,d) $AoA = 11^{\circ}$; (e,f) $AoA = 14^{\circ}$;

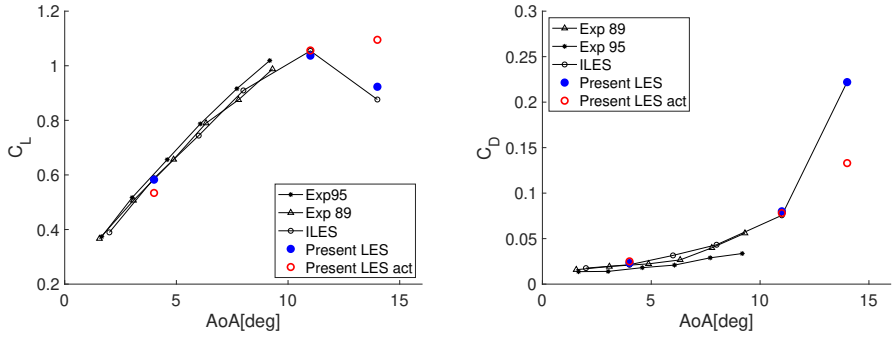

(a) (b)

Fig. 6: Aerodynamic coefficients at different angles of attack. Comparison between actuated and baseline cases. Literature results for the baseline cases are also included ILES (Galbraith & Visbal 2008), Exp89 (Selig et al. 1989), Exp95 (Selig et al. 1995). (a) Lift coefficient. (b) Drag coefficient.

(figure 5c,d). Downstream the reattachment point, the pressure recovery and the skin friction coefficient behave similarly for both the baseline and actuated cases.

At $AoA = 14^{\circ}$, differences between the baseline and actuated cases are quite important. While the former corresponds with a stalled airfoil (see the typical flat pressure profile along the suction side indicating a large recirculation zone, figure 5e), the latter presents a different behaviour. As in the previous cases, the periodic actuation close to the leading edge transfers momentum to the flow and produces three-dimensional instabilities which trigger the transition to turbulence. When the turbulent boundary layer separates, the added momentum forces the shear layer to reattach to the airfoil surface at about $x/C = 0.13$ and the flow remains attached for most of the airfoil chord. Actually, the further detachment of the flow occurs at $x/C = 0.67$, where a small recirculation zone is formed (see figure 5e,f).

Table 1: Aerodynamic coefficients for the baseline and actuated cases at different angles of attack. C_d drag coefficient, $C_{d,p}$ and $C_{d,f}$ form and friction drag, $C_{d,rms}$ drag coefficient fluctuations, C_L lift coefficient, $C_{L,p}$ and $C_{L,f}$ form and friction lift, $C_{L,rms}$ lift coeffiicient fluctuations.

	C_d	$C_{d,p}$	$C_{d,f}$	$C_{d,rms}$	C_L	$C_{L,p}$	$C_{L,f}$	$C_{L,rms}$
				$AoA = 4^\circ$				
Baseline	0.023	0.013	0.010	0.001	0.583	0.582	0.001	0.006
Actuated	0.025	0.011	0.014	0.001	0.533	0.533	0.000	0.004
				$AoA = 11^\circ$				
Baseline	0.080	0.072	0.008	0.006	1.035	1.034	0.001	0.020
Actuated	0.078	0.068	0.010	0.003	1.056	1.055	0.001	0.010
				$AoA = 14^\circ$				
Baseline	0.238	0.232	0.006	0.027	0.886	0.885	0.001	0.116
Actuated	0.129	0.122	0.007	0.007	1.078	1.077	0.001	0.042

The periodic actuation has a direct impact in the aerodynamic forces in the airfoil, especially at post-stall angles of attack. In figure 6 drag and lift coefficients at the angles-of-attack considered in the present study are plotted against the baseline case. In the figure, reference values from the experiments performed by Selig et al. (1989, 1995) and from the ILES by Galbraith & Visbal (2008) are also included. In addition, in table 1 the values of these forces together with the form and viscous contribution are given. At low angles-of-attack, although the actuation successfully eliminates the laminar separation bubble, it offers no advantages from the airfoil aerodynamic efficiency point of view ($(C_L/C_d)_{base} = 25.3$ vs. $(C_L/C_d)_{act} = 21.3$). In fact, efficiency slightly decreases and the elimination of the LSB slightly increases the viscous contribution to the drag. These results

are in disagreement with the observations of Goodfellow et al. (2013) for a NACA 0025 at $AoA = 5^{\circ}$, who found that the actuation reduces the drag and the wake width behind the airfoil. However, this apparently contradictory result might be related with the airfoil design. NACA 0025 is a thick symmetric airfoil with trailing edge separation, whereas SD7003 is a cambered airfoil especially designed to have a shallow LSB with leading edge separation. In fact, Selig et al. (1989) pointed out that SD7003 airfoil was designed so as to have a LSB with a gradual pressure recovery. Thus, for this design the elimination of the LSB produces no benefit from the drag point of view. This is also in agreement with the Selig et al. (1989) experimental results in which they observed that tripping the boundary layer and triggering transition did not reduce the airfoil drag.

Conversely, at post-stall angle of attack $AoA = 14^{\circ}$, the benefits from the actuation are very clear. It retards the stall by eliminating the large recirculation zone and promoting the flow reattachment, and as a consequence, the lift coefficient increases by 22%, whereas the reduction in the drag forces is about 46%, thus increasing the airfoil aerodynamic efficiency by 124%. Moreover, the actuation reduces the fluctuations in both lift and drag forces at all AoAs. This is specially interesting at the larger AoA as the transient flow is dominated by the shedding of vortices. When the periodic actuation is active, and as a consequence of the flow reattachment, fluctuations are reduced by a 74% and 64% in the drag and lift forces, respectively.

3.2 Effect of the actuation on the average flow

In table 2 the average streamwise location of the separation x_{sep}/C, transition to turbulence x_{tra}/C and reattachment of the flow x_{reat}/C are given. Separation is defined as the point where the tangential velocity and the wall shear stress become zero and $\partial\tau_w/\partial s < 0$ (s being the airfoil tangential direction). In a similar manner reattachment is defined as the location where the tangential velocity and the wall shear stress become zero and $\partial\tau_w/\partial s > 0$. For finding the average transition location, different methods can be found in the literature. For instance, Alam & Sandham (2000) defined the transition point as the location where the skin friction coefficient reaches its minimum value. Boutilier & Yarusevych (2012) proposed to use the location where the zone of almost constant C_p in the suction side ends. Istvan & Yarusevych (2018) used the location of the maximum displacement thickness. Considering that Reynolds shear stress is a magnitude that quantify the exchange of momentum, the average transition location can be determined based on a threshold value of $< -u'v'/U_\infty^2 >= 0.001$. The latter has been widely used in the literature for determining the location of the transition point (see for instance (Ol et al. 2005, Galbraith & Visbal 2008, Hain et al. 2009)) and is the one used in the present work. Complementing the table, the data of separation and reattachment, when apply, are also plotted in figure 7. In addition, in figure 8 the averaged streamlines coloured by the Reynolds shear stresses are also depicted, whereas in figure 9 the boundary layer thickness and shape factor are plotted. Here, the boundary layer thickness δ_{95} is defined as the location where the velocity is 95% of the edge velocity ($U_e = max(U)$) and the shape factor is $H = \delta_1/\delta_2$, δ_1 and δ_2 being the displacement and momentum boundary layer thicknesses, respectively;

Table 2: Streamwise location of the separation (x_{sep}/C, transition to turbulence (x_{tra}/C) and reattachment (x_{reat}/C)

	x_{sep}/C	x_{tra}/C	x_{reat}/C
Baseline			
$AoA = 4^\circ$	0.241	0.527	0.670
$AoA = 11^\circ$	0.008	0.057	0.146
$AoA = 14^\circ$	0.012	0.131	-
Actuated			
$AoA = 4^\circ$	-	0.016	-
$AoA = 11^\circ$	0.048	0.017	0.096
$AoA = 14^\circ$	0.042	0.037	0.123

δ_1 and δ_2 are defined as

$$\delta_1 = \int_0^{\delta_{95}} \left(1 - \frac{U}{U_e}\right) dy; \quad \delta_2 = \int_0^{\delta_{95}} \frac{U}{U_e}\left(1 - \frac{U}{U_e}\right) dy. \tag{5}$$

Notice that in figure 9, boundary layer thickness and shape factor at $AoA = 14^\circ$ are not given for the baseline case as the flow is separated for most of the airfoil chord.

It is important to remark that for all cases transition to turbulence location moves upstream if compared with the baseline cases. Moreover, based on the estimation of the transition point, the actuation changes the transition to turbulence mechanism (see values reported in table 2). For the baseline cases, transition to turbulence occurs in the separated shear layer; however when the periodic actuation is activated transition to turbulence occurs before actual separation of the boundary layer does occur, i.e. transition to turbulence occurs on the airfoil surface.

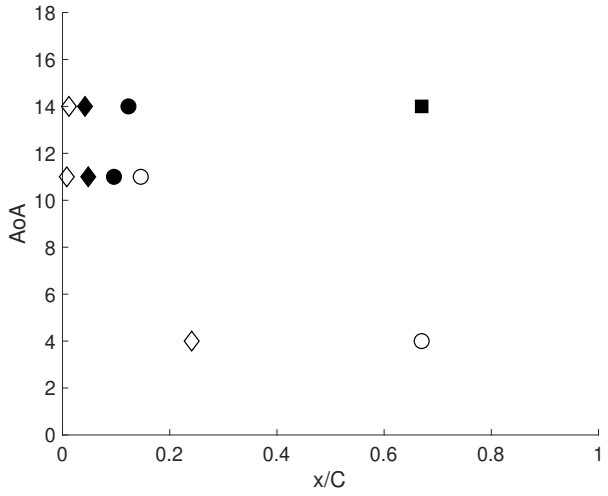

Fig. 7: Location of the separation (diamonds) and reattachment (circles) points for both baseline (empty symbols) and actuated (solid symbols) cases. Turbulent boundary layer separation at $AoA = 14^{\circ}$ is marked with a solid square.

At $AoA = 4^{\circ}$, as commented before, for the baseline case a LSB is formed, whereas it is successfully eliminated for the actuated case, as can also be seen from the contours of the Reynolds shear stresses (see figure 8a,b). As a consequence, the boundary layer shape factor profile changes completely (see figure 9b). For the baseline case, the presence of the LSB can also be inferred from the profile of the shape factor with transition to turbulence occurring about the peak in the shape factor; after the reattachment of the flow ($x_{reat} = 0.67$) a turbulent boundary layer is developed. For the actuated case, as transition to turbulence occurs close to the leading edge, a turbulent boundary layer is developed for almost the whole airfoil chord as can be seen from figure 9. Notice also the almost flat profile of the shape factor. For the point of maximum lift, i.e. $AoA = 11^{\circ}$, the behaviour of

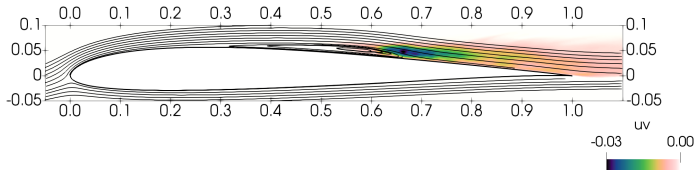

(a)

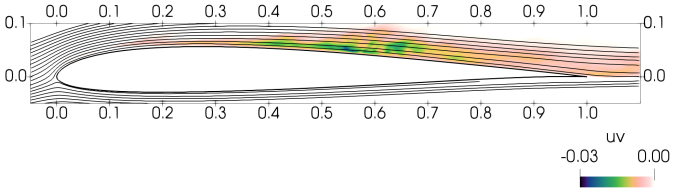

(b)

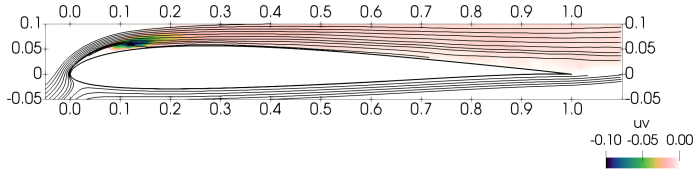

(c)

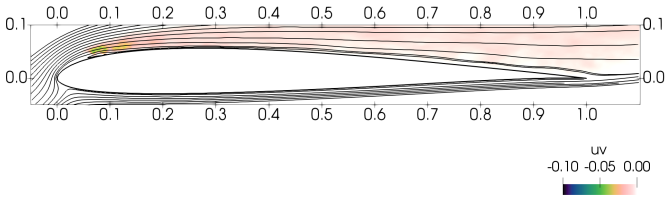

(d)

Fig. 8: Streamlines and contours of the non-dimensional shear stresses $< u'v' >$ $/U_\infty^2$ for the baseline and actuated cases. (a) $AoA = 4^\circ$ baseline; (b) $AoA = 4^\circ$ actuated ; (c) $AoA = 11^\circ$ baseline; (d) $AoA = 11^\circ$ actuated; (e)$AoA = 14^\circ$ baseline; (f) $AoA = 14^\circ$ actuated.

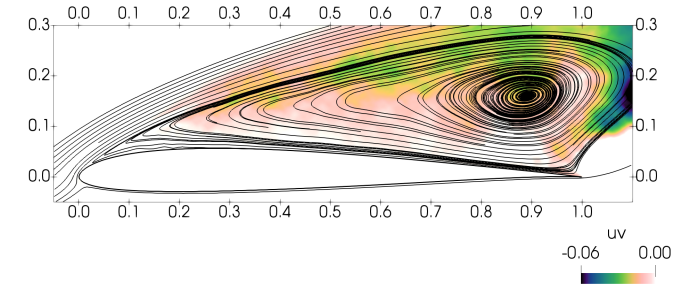

(e)

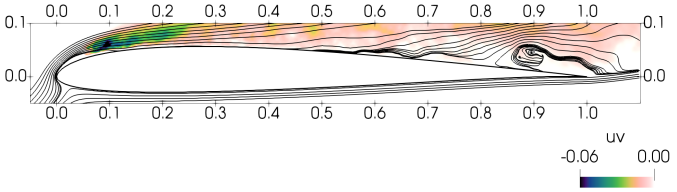

(f)

Fig. 8: (cont) Streamlines and contours of the non-dimensional shear stresses $< u'v' > /U_\infty^2$ for the baseline and actuated cases. (a) $AoA = 4^\circ$ baseline; (b) $AoA = 4^\circ$ actuated ; (c) $AoA = 11^\circ$ baseline; (d) $AoA = 11^\circ$ actuated; (e)$AoA = 14^\circ$ baseline; (f) $AoA = 14^\circ$ actuated.

both the baseline and the actuated cases is pretty similar. The main differences are in the nature of the small recirculation bubble formed close to the leading edge. While for the baseline case, separation is laminar and reattachment occurs as a consequence of the transition to turbulence, in the actuated case there is a turbulent separation. In this case, as was explained by Tuck & Soria (2008), the large scale structures injected by the actuator retard the separation and, enhance the entrainment of the shear layer, whereas at the same time the vortices formed transfer momentum to deflect the turbulent shear layer towards the airfoil surface.

As a result, a smaller recirculation is formed on the airfoil surface. Notice also that the profile of the shape factor changes in the separated zone, but after separation the boundary layer of both the actuated and the baseline cases behaves in a similar manner.

The largest changes occur at $AoA = 14^{\circ}$. The baseline case is characterised by a large recirculation bubble occupying the whole airfoil surface, typical of airfoils that exhibit bubble bursting and leading edge stall (see for instance Rodríguez et al. (2013)). However, the periodic actuation produces a small recirculation bubble close to the leading edge and with similar characteristics to the one formed at $AoA = 11^{\circ}$. Although the actuation is capable of suppressing the massive separation at this angle, the turbulent boundary layer eventually separates towards the trailing edge at $x_{sep}/C = 0.67$. This location is also marked in figure 9 by a black dot. In other words, the periodic actuation changes the flow separation at this angle-of-attack from a laminar separation near the leading edge of the airfoil to a turbulent separation close to the rear of the airfoil. Actually a closer look at the pressure profile shown in figure 5e shows that pressure does not recover at the same ratio as in $AoA = 11^{\circ}$ and flattens in the rear end region, which is which is also indicative of the recirculation formed close to the trailing edge (see also figure 8f). Moreover, turbulent transition moves forward the point where the small recirculation bubble in the leading edge is placed. This behaviour, is more typical of the airfoils that exhibit combined trailing-edge/leading-edge stall (this type of stall is more characteristic of medium-thickness airfoils and higher Reynolds numbers (Polhamus 1996)) rather than the leading-edge stall characteristic of the SD7003. In other words, the injected momentum retards the leading edge bubble bursting while trailing edge separation starts to occur, which is typ-

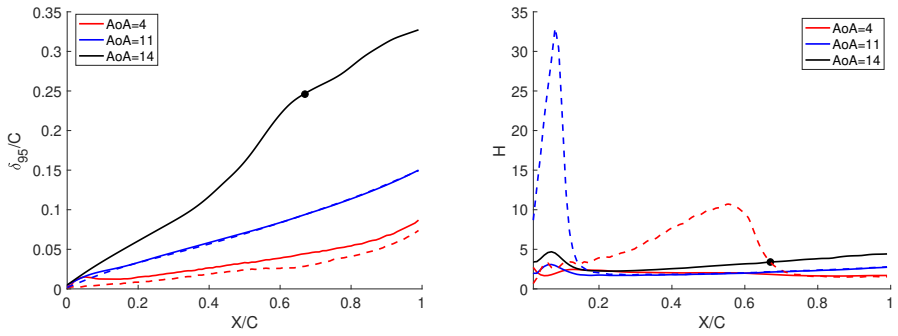

(a) (b)

Fig. 9: (a) Boundary layer thickness and (b) shape factor for the actuated cases. Comparison for the different angles of attack. The solid dot represents the boundary layer separation for the actuated case at $AoA = 14^{\circ}$. Baseline cases (dashed lines), actuated cases (solid lines).

ical of the trailing-edge/leading edge type of stall. It is conjectured that if the angle-of-attack is further increased, the recirculation zone will move towards the leading edge and, eventually, when it approaches about airfoil mid-chord it will reach the new maximum lift angle.

A further insight into the effects of the actuation on the flow can be given by the inspection of the velocity profiles in the wake (see figures 10 and 11) and on the average flow statistics along the airfoil chord (see figure 12). These profiles are only shown at $AoA = 14^{\circ}$ where the effect of the actuation is effectively noticeable. Wake velocity profiles are compared at three locations downstream the airfoil trailing edge at $x/C = 1.2$, 1.5, 2 for the baseline and the actuated cases. As can be seen from figures 10 and 11, as a consequence of the reduction of the separated zone in both chord-wise length and bubble height, there is much less irrotational fluid

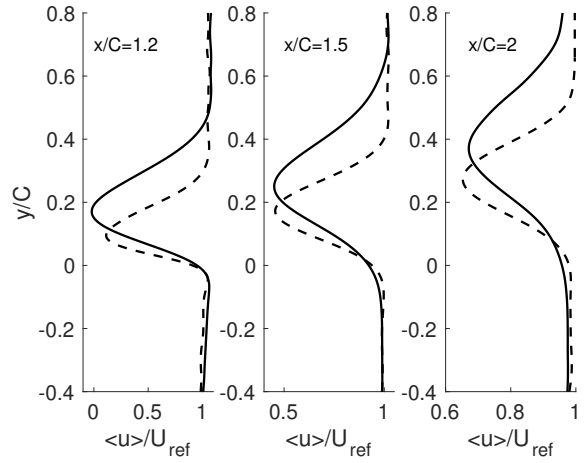

Fig. 10: Wake streamwise velocity profiles at different locations. Comparison for the baseline (solid lines) and actuated (dashed lines) cases for $AoA = 14^{\circ}$.

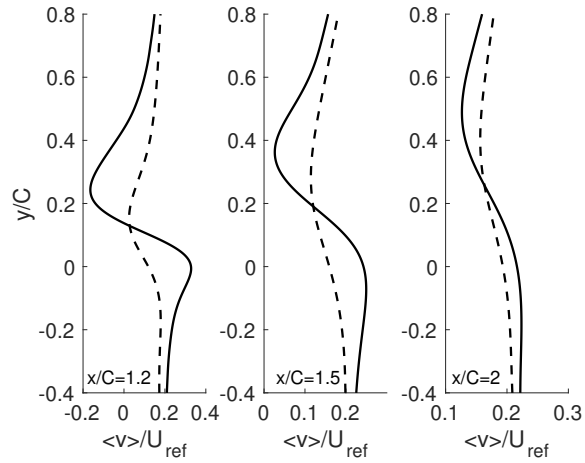

Fig. 11: Wake cross-stream velocity profiles at different locations. Comparison for the baseline (solid lines) and actuated (dashed lines) cases for $AoA = 14^{\circ}$.

entrainment, the wake width is reduced and the maximum velocity deficit is moved downwards towards lower y/C values. This is also indicative of the reduction in the drag achieved (see also figure 6b).

In order to provide evidence on the effect on the turbulent flow, figure 12 depicts the streamwise velocity, and Reynolds stresses at different wall-normal locations on the suction side at $x/C = 0.4$, 0.5, 0.6, 0.7, 0.8, 0.9. The mean streamwise velocity shows the large separated region for the baseline case and how for $x/C < 0.7$ the flow is attached to the airfoil surface for the actuated case. However, even when the flow separates close to the rear end of the airfoil, as it is commented before, the reverse flow region is effectively reduced in the actuated case. Moreover, the inspection of the Reynolds stresses profiles shows a change in the turbulent fluctuations of the flow. The actuation not only reduces the extent of the recirculation zone but it also diminishes the turbulent fluctuations of the flow and introduces a shift in the location of the peaks towards the airfoil surface, the region of turbulent fluctuations in the baseline case being larger than in the actuated one.

4 Conclusions

The effects on the laminar separation bubble and on the separated shear layer of a periodic in time and space synthetic jet actuator have been studied by means of large-eddy simulations. The SD7003 airfoil at a Reynolds number of 6×10^4 and angles of attacks of $AoA = 4^\circ$, 11°, 14° has been here the focus of interest. The results show that applying a periodic actuation with $F^+ = 1$ and $C_\mu = 3 \times 10^{-3}$ successfully eliminates the laminar separation bubble at $AoA = 4^\circ$; however, due to the added viscous drag it does not result in a reduction of the drag coefficient.

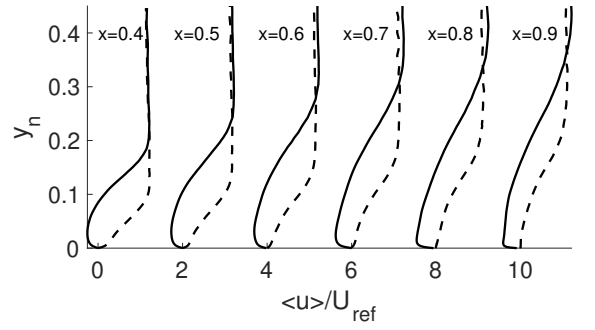

(a)

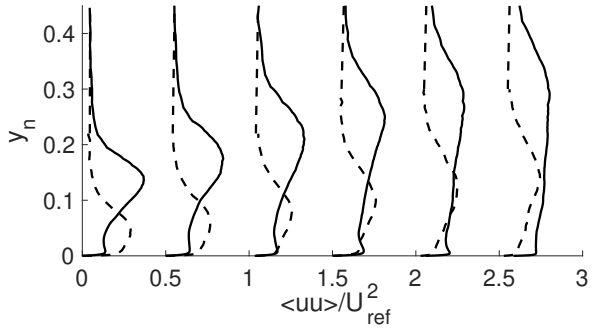

(b)

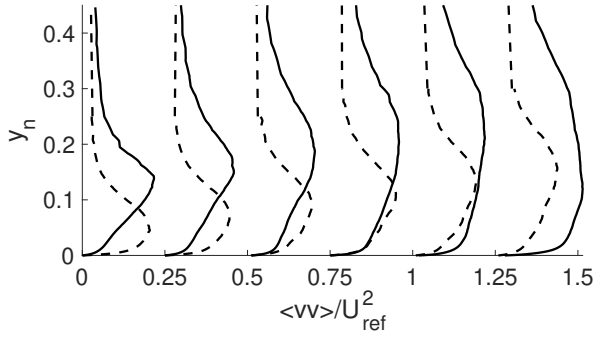

(c)

Fig. 12: (a) Streamwise velocity, (b) streamwise Reynolds stresses, (c) wall-normal Reynolds stresses, (d) Reynolds shear stresses. Comparison for the baseline (solid line) and actuated (dashed line) at different surface normal locations for $AoA = 14°$.

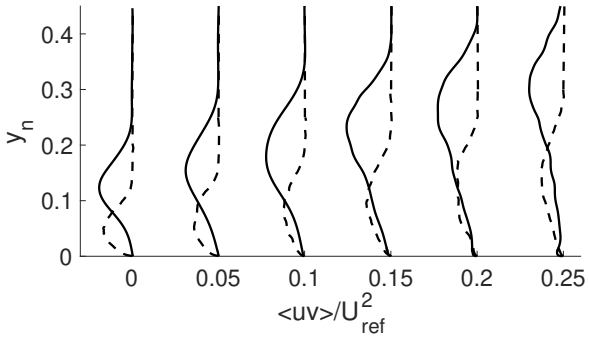

(d)

Fig. 12: (a) Streamwise velocity, (b) streamwise Reynolds stresses, (c) wall-normal Reynolds stresses, (d) Reynolds shear stresses. Comparison for the baseline (solid line) and actuated (dashed line) at different surface normal locations for $AoA = 14^{\circ}$.

In terms of airfoil aerodynamic efficiency, the actuation is only effective at angles of attack larger than the point of maximum lift, where it eliminates the massive flow separation and delays the airfoil stall. At $AoA = 14^{\circ}$, the periodic actuation suppresses the large recirculation and forces the shear layer to reattach to the airfoil surface, and as a consequence, it also increases the airfoil lift by 22% and reduces the drag by 46% resulting in an increase in the airfoil aerodynamic efficiency by a 124%.

Important effects on the flow are also observed. As a consequence of the actuation, the transition to turbulence mechanism changes from a KH instability in the separated shear layer to occur right after the actuator outlet on the airfoil surface. It is also shown that at larger angles of attack, the reduction in the separated flow decreases the wake width, which is also indicative of the drag reduction, displacing

the maximum velocity deficit towards lower y/C values, and decreases the turbulent fluctuations of the flow. Moreover, the injected momentum produces a small recirculation bubble close to the airfoil leading edge and retards separation of the boundary layer at larger angles of attack. Thus, turbulent separation occurs close to the rear end of the airfoil, with a recirculation zone that flattens the pressure profile. It is conjectured that the combination of the small recirculation bubble in the leading edge with the turbulent boundary layer separation past airfoil mid-chord might lead to a trailing-edge/leading-edge type of stall at larger angles of attack. Thus, it is suggested that the actuation changes the nature of the stall to a trailing-edge/leading-edge stall more typical of medium-thickness airfoils rather than the leading-edge type of stall of the SD7003.

Compliance with Ethical Standards

The authors declare that they have no conflict of interest.

Acknowledgments

This work has been partially financially supported by the Ministerio de Economía y Competitividad, Secretaría de Estado de Investigación, Desarrollo e Innovación, Spain (Ref. TRA2017-88508-R) and by European Union's Horizon 2020 research and innovation programme (INFRAEDI-02-2018, EXCELLERAT- The European Centre Of Excellence For Engineering Applications H2020.). We also acknowledge Red Española de Surpercomputación (RES) for awarding us access to the MareNostrum IV machine based in Barcelona, Spain (Ref. FI-2018-2-0015 and

FI-2018-3-0021).This work is also funded in part by the Coturb program of the European Research Council.

References

Akbarzadeh, A. & Borazjani, I. (2019), A numerical study on controlling flow separation via surface morphing in the form of backward traveling waves, *in* 'AIAA Aviation Forum', pp. 1–11.

Alam, M. & Sandham, N. (2000), 'Direct numerical simulation of short separation bubbles with turbulent reattachment', *Journal of Fluid Mechanics* **410**, 1–28.

Albers, M., Meysonnat, P. S. & Schröder, W. (2019), 'Actively Reduced Airfoil Drag by Transversal Surface Waves', *Flow, Turbulence and Combustion* **102**(4), 865–886.

Amitay, M. & Glezer, a. (2002), 'Role of actuation frequency in controlled flow reattachment over a stalled airfoil', *AIAA Journal* **40**(2), 209–216.

Amitay, M., Smith, D. R., Kibens, V., Parekh, D. E. & Glezer, A. (2001), 'Aerodynamic flow control over an unconventional airfoil using synthetic jet actuators', *AIAA journal* **39**(3), 361–370.

Atzori, M., Vinuesa, R., Stroh, A., B.Frohnapfel & Schlatter., P. (2018), Assessment of skin-friction-reduction techniques on a turbulent wing section, *in* 'ETMM-12 2018'.

Boutilier, M. S. H. & Yarusevych, S. (2012), 'Parametric study of separation and transition characteristics over an airfoil at low Reynolds numbers', *Experiments in Fluids* **52**(6), 1491–1506.

Buchmann, N. A., Atkinson, C. & Soria, J. (2013), 'Influence of ZNMF jet flow control on the spatio-temporal flow structure over a NACA-0015 airfoil', *Experiments in Fluids* **54**(3).

Calmet, H., Gambaruto, A. M., Bates, A. J., Vázquez, M., Houzeaux, G. & Doorly, D. J. (2016), 'Large-scale CFD simulations of the transitional and turbulent regime for the large human airways during rapid inhalation', *Computers in biology and medicine* **69**(1), 166–180.

Cattafesta, L. N. & Sheplak, M. (2011), 'Actuators for Active Flow Control', *Annual Review of Fluid Mechanics* **43**(1), 247–272.

Charnyi, S., Heister, T., Olshanskii, M. A. & Rebholz, L. G. (2017), 'On conservation laws of navier-stokes galerkin discretizations', *J. Comput. Phys.* **337**, 289 – 308.

Choi, K. S., Timothy, J. & Whalley, R. (2011), 'Turbulent boundary-layer control with plasma actuators', *Philosophical Transactions of the Royal Society A: Mathematical, Physical and Engineering Sciences* **369**(1940), 1443–1458.

Codina, R. (2001), 'Pressure stability in fractional step finite element methods for incompressible flows', *J. Comput. Phys.* **130**(1), 112–140.

Duvigneau, R. & Visonneau, M. (2006), 'Optimization of a synthetic jet actuator for aerodynamic stall control', *Computers and Fluids* **35**(6), 624–638.

Eto, K., Kondo, Y., Fukagata, K. & Tokugawa, N. (2018), *Friction Drag Reduction on a Clark-Y Airfoil Using Uniform Blowing.*

URL: *https://arc.aiaa.org/doi/abs/10.2514/6.2018-3374*

Galbraith, M. & Visbal, M. (2008), 'Implicit Large Eddy Simulation of Low Reynolds Number Flow Past the SD7003 Airfoil', *46th AIAA Aerospace Sciences Meeting and Exhibit* (January), 1–17.

Gilarranz, J. L., Traub, L. W. & Rediniotis, O. K. (2005*a*), 'A New Class of Synthetic Jet Actuators—Part I: Design, Fabrication and Bench Top Characterization', *Journal of Fluids Engineering* **127**(2), 367.

Gilarranz, J. L., Traub, L. W. & Rediniotis, O. K. (2005*b*), 'A New Class of Synthetic Jet Actuators—Part II: Application to Flow Separation Control', *Journal of Fluids Engineering* **127**(2), 377.

Glezer, A. (2011), 'Some aspects of aerodynamic flow control using synthetic-jet actuation', *Philosophical Transactions of the Royal Society A: Mathematical, Physical and Engineering Sciences* **369**(1940), 1476–1494.
URL: *http://rsta.royalsocietypublishing.org/cgi/doi/10.1098/rsta.2010.0374*

Goodfellow, S. D., Yarusevych, S. & Sullivan, P. E. (2013), 'Momentum coefficient as a parameter for aerodynamic flow control with synthetic jets', *AIAA Journal* **51**(3), 623–631.

Gövert, S., Mira, D., Zavala-Ake, M., Kok, J., Vázquez, M. & Houzeaux, G. (2017), 'Heat loss prediction of a confined premixed jet flame using a conjugate heat transfer approach', *International Journal of Heat and Mass Transfer* **107**, 882 – 894.

Hain, R., Kähler, C. J. & Radespiel, R. (2009), 'Dynamics of laminar separation bubbles at low-Reynolds-number aerofoils', *Journal of Fluid Mechanics* **630**, 129–153.

Huang, L., Huang, P. G., LeBeau, R. P. & Hauser, T. (2004), 'Numerical study of blowing and suction control mechanism on NACA0012 airfoil', *Journal of Aircraft* **41**(5), 1005–1013.

Hunt, J., Wray, A. & Moin, P. (1988), Eddies, stream and convergence zones in turbulent flows, Technical Report CTR-S88, Center for turbulent research.

Istvan, M. S. & Yarusevych, S. (2018), 'Effects of free-stream turbulence intensity on transition in a laminar separation bubble formed over an airfoil', *Experiments in Fluids* **59**(3), 1–21.

URL: *http://dx.doi.org/10.1007/s00348-018-2511-6*

Kim, J., Moin, P. & Seifert, A. (2017), 'Large-eddy simulation-based characterization of suction and oscillatory blowing fluidic actuator', *AIAA Journal* **55**(8), 2566–2579.

Kitsios, V., Cordier, L., Bonnet, J.-P., Ooi, a. & Soria, J. (2011), 'On the coherent structures and stability properties of a leading-edge separated aerofoil with turbulent recirculation', *Journal of Fluid Mechanics* **683**(2011), 395–416.

Lehmkuhl, O., Houzeaux, G., Owen, H., Chrysokentis, G. & Rodriguez, I. (2019), 'A low-dissipation finite element scheme for scale resolving simulations of turbulent flows', *Journal of Computational Physics* **390**, 51–65.

Liu, P. Q., Duan, H. S., Chen, J. Z. & He, Y. W. (2010), 'Numerical study of suction-blowing flow control technology for an airfoil', *Journal of Aircraft* **47**(1), 229–239.

McCormick, D. C. (2000), Boundary Layer Separation control with Directed Synthetic Jets, *in* '38th Aerospace Sciences Meeting & Exhibit', number AIAA 2000-0519.

Mira, D., Zavala-Ake, M., Avila, M., Owen, H., Cajas, J. C., Vazquez, M. & Houzeaux, G. (2016), 'Heat transfer effects on a fully premixed methane impinging flame', *Flow, Turbulence and Combustion* **97**(1), 339–361.

Mueller, T. J. & DeLaurier, J. D. (2003), 'Aerodynamics of small vehicles', *Annual Review of Fluid Mechanics* **35**(1), 89–111.

Ol, M., McAuliffe, B., Hanff, E., Scholz, U. & Kähler, C. (2005), Comparison of Laminar Separation Bubble Measurements on a Low Reynolds Number Airfoil in Three Facilities, *in* '35th AIAA Fluid Dynamics Conference and Exhibit'.

Pastrana, D., Cajas, J. C., Lehmkuhl, O., Rodríguez, I. & Houzeaux, G. (2018), 'Large-eddy simulations of the vortex-induced vibration of a low mass ratio two-degree-of-freedom circular cylinder at subcritical reynolds numbers', *Comput. Fluids.* **173**, 118–132.

Polhamus, E. C. (1996), A Survey of Reynolds Number and Wing Geometry Effects on Lift Characteristics in the Low Speed Stall Region, Technical report.

Rodríguez, I., Lehmkuhl, O., Borrell, R. & Oliva, a. (2013), 'Direct numerical simulation of a NACA0012 in full stall', *International Journal of Heat and Fluid Flow* **43**, 194–203.

Rodriguez, I., Lehmkuhl, O., Soria, M., Gomez, S., Domınguez-Pumar, M. & Kowalski, L. (2019), 'Fluid dynamics and heat transfer in the wake of a sphere', *International Journal of Heat and Fluid Flow* **76**(C), 141–153.

Sandham, N. D. (2008), 'Transitional separation bubbles and unsteady aspects of aerofoil stall', **112**(1133), 395–404.

Schmidt, S. & Breuer, M. (2014), 'Hybrid LES-URANS methodology for the prediction of non-equilibrium wall-bounded internal and external flows', *Computers and Fluids* **96**, 226–252.

Selig, Donovan & Fraser (1989), Airfoils at Low Speeds, Technical report, University of Illinois.

Selig, M., Guglielmo, J. J., Broeren, A. P. & Giguere, P. (1995), Summary of Low-Speed Airfoil Data Summary of Low-Speed Airfoil Data, Technical report, University of Illinois.

Trias, F. X. & Lehmkuhl, O. (2011), 'A self-adaptive strategy for the time integration of Navier-Stokes equations', *Numerical Heat Transfer. Part B* **60**(2), 116–134.

Tuck, A. & Soria, J. (2008), 'Separation control on a NACA 0015 airfoil using a 2D micro ZNMF jet', *Aircraft Engineering and Aerospace Technology* **80**(2), 175–180.

Vázquez, M., Houzeaux, G., Koric, S., Artigues, A., Aguado-Sierra, J., Arís, R., Mira, D., Calmet, H., Cucchietti, F., Owen, H., Taha, A., Burness, E. D., Cela, J. M. & Valero, M. (2016), 'Alya: Multiphysics engineering simulation toward exascale', *Journal of Computational Science* **14**, 15–27.

Vreman, A. W. (2004), 'An eddy-viscosity subgrid-scale model for turbulent shear flow: Algebraic theory and applications', *Physics of Fluids* **16**(10), 3670–3681.

You, D. & Moin, P. (2008), 'Active control of flow separation over an airfoil using synthetic jets', *Journal of Fluids and Structures* **24**(8), 1349–1357.

Zheng, J., Cui, Y. D., Zhao, Z., Li, J. M. & Khoo, B. C. (2018), 'Flow separation control over a NACA 0015 airfoil using nanosecond-pulsed plasma actuator', *AIAA Journal* **56**(6), 2220–2234.

Zhu, H., Hao, W., Li, C., Ding, Q. & Wu, B. (2019), 'Application of flow control strategy of blowing, synthetic and plasma jet actuators in vertical axis wind turbines', *Aerospace Science and Technology* **88**, 468–480.